Monthly Notices of the ROYAL ASTRONOMICAL SOCIETY

MNRAS **543,** 1761–1774 (2025) https://doi.org/10.1093/mnras/staf1542
Advance Access publication 2025 September 13

Quantifying the intrinsic variability due to randomness of the Auriga galaxy formation model

Rüdiger Pakmor [1]★ Rebekka Bieri [2] Francesca Fragkoudi [3] Facundo A. Gómez [4] Robert J. J. Grand [5] Christine M. Simpson [6] Rosie Y. Talbot [1] Freeke van de Voort [7] and Maria Werhahn [1]

[1]*Max-Planck-Institut für Astrophysik, Karl-Schwarzschild-Str 1, D-85748 Garching, Germany*
[2]*Department of Astrophysics, University of Zurich, 8057 Zurich, Switzerland*
[3]*Institute for Computational Cosmology, Department of Physics, Durham University, South Road, Durham DH1 3LE, UK*
[4]*Departamento de Astronomía, Universidad de La Serena L3 5RF, Av. Juan Cisternas 1200 Norte, La Serena, Chile*
[5]*Astrophysics Research Institute, Liverpool John Moores University, 146 Brownlow Hill, Liverpool L3 5RF, UK*
[6]*Argonne Leadership Computing Facility, Argonne National Laboratory, Lemont, IL 60439, USA*
[7]*Cardiff Hub for Astrophysics Research and Technology, School of Physics and Astronomy, Cardiff University, Queen's Buildings, Cardiff CF24 3AA, UK*

Accepted 2025 September 10. Received 2025 September 10; in original form 2025 July 17

ABSTRACT

Numerical simulations have become an indispensable tool in astrophysics. To interpret their results, it is critical to understand their intrinsic variability, i.e. how much the results change with numerical noise or inherent stochasticity of the physics model. We present a set of seven realizations of high-resolution cosmological zoom-in simulations of a Milky Way-like galaxy with the Auriga galaxy formation model. All realizations share the same initial conditions and code parameters, but draw different random numbers for the inherently stochastic parts of the model. We show that global galaxy properties at $z = 0$, including stellar mass, star formation history, masses of stellar bulge and stellar disc, the radius and height of the stellar disc change by less than 10 per cent between the different realizations, and that magnetic field structures in the disc and the halo are very similar. In contrast, the star formation rate today can vary by a factor of 2, and the internal morphological structure of the stellar disc can change. The time and orbit of satellite galaxies and their galaxy properties when falling into the main halo are again very similar, but their orbits start to deviate after the first pericentre passage. Finally, we show that changing the mass resolution of all matter components by a factor of 8 in the Auriga model changes galaxy properties significantly more than the intrinsic variability of the model, and that these changes are systematic. This limits detailed comparisons between simulations at different numerical resolutions.

Key words: hydrodynamics – methods: numerical.

1 INTRODUCTION

Galaxies are complex systems governed by many different physical processes that are often strongly coupled. Numerical simulations are an indispensable tool to model these physical processes and their interactions in detail to obtain a full picture of the formation and evolution of galaxies. Cosmological simulations in particular are critical, because they allow us to self-consistently model galaxies in their full environment and over entire cosmic history (Vogelsberger et al. 2020; Crain & van de Voort 2023).

Recent cosmological galaxy simulations produce galaxy populations generally consistent with observations (Vogelsberger et al. 2014; Schaye et al. 2015; Dubois et al. 2016; Springel et al. 2018; Davé et al. 2019; Pakmor et al. 2023). Comparison with observations usually focuses on ensemble averages between a population of simulated galaxies and a population of observed galaxies. Ideally, this averages out galaxy-to-galaxy variability from selection effects. Moreover, it also reduces the impact of variability intrinsic to the simulations. However, the robustness of properties of simulated galaxies is hard to judge for individual galaxies, and the intrinsic variability is likely significant for many galaxy formation models (Genel et al. 2019; Keller et al. 2019; Borrow et al. 2023).

Quantifying the impact of specific physical processes from simulations of a large number of galaxies at reasonable resolution is computationally unfeasible, because every single box is expensive already (Nelson et al. 2019; Villaescusa-Navarro et al. 2021). Therefore, galaxy simulations focusing on the study of physical processes by comparing simulations run with different physics models or parameters usually only simulate a small number of galaxies with a zoom-in approach. This way, they focus essentially all resolution elements in one main galaxy of interest. They then simulate the same galaxy multiple times with different physical models, for example, to understand the impact of magnetic fields on galaxies (Pakmor et al. 2017; Whittingham et al. 2021, 2023) and the circumgalactic medium (van de Voort et al. 2021), cosmic rays (Buck et al. 2020; Hopkins

★ E-mail: rpakmor@mpa-garching.mpg.de

et al. 2020; Martin-Alvarez et al. 2023; Rodríguez Montero et al. 2024; Bieri et al. 2025), different supermassive black hole models (see e.g. Irodotou et al. 2022), or the impact of systematic variations of the assembly history of a galaxy (Davies, Crain & Pontzen 2021; Davies, Pontzen & Crain 2022; Rey et al. 2023; Joshi et al. 2024). Then, however, it becomes critical to understand the robustness of the simulations for individual galaxies.

A fundamental source of variability for essentially all numerical simulations is that floating-point operations do not commute. Rather, the exact result will depend on the order of operations, for example, the order in which various partial forces are added up to a total force. Genel et al. (2019) showed that while these differences are initially tiny, they can grow quickly for sufficiently chaotic systems. Moreover, they demonstrated that even though a tiny change in the simulation in one place will not change the properties of a large population of galaxies very much, individual galaxies can eventually look very different.

A much more important source of variability for galaxy formation simulations, which also significantly amplifies variability from round-off errors, is stochastic operations built into the model, for example, in the models for star formation of stellar feedback. Because galaxy formation includes many physical processes that are strongly coupled, any local deviation, for example, because a different set of random numbers is drawn, will quickly propagate. Any change of the random number seed (that changes the set of random numbers used) or round-off errors (e.g. because we use a different number of tasks or a different machine to run on) will produce equally valid results for a given code and model. We can therefore use a set of simulations of the same initial conditions with the same code and model parameters, but different random number seeds, to quantify the intrinsic variability of a simulation.

Despite the fundamental importance of galaxy physics studies, little work has been done focusing on the intrinsic variability of galaxy simulations. Keller et al. (2019) studied the intrinsic variance in simulations of isolated dwarf galaxies and cosmological simulations of Milky Way-like galaxies. Using different feedback models, they ran pairs of dwarf galaxies with the same model and resimulated a dwarf galaxy with one model 128 times. They found a typical relative variation in stellar mass after 1 Gyr of 5–10 per cent, with differences up to a factor of 2 in extreme cases. They also evolved pairs of Milky Way-like galaxies with different feedback models in a fully cosmological setting to $z = 0.9$. There, they found significantly larger deviations in stellar mass compared to the isolated dwarf galaxies, with persisting differences in stellar mass larger than 10 per cent. They also show that the galaxies can appear qualitatively different.

Focusing on the impact of systematic modifications to the initial conditions, Davies et al. (2021, 2022) ran nine realizations of one cosmological zoom simulation with different random number seeds for five sets of initial conditions to disentangle the intrinsic variability of the EAGLE galaxy formation model (Schaye et al. 2015) from the effect of modifying the initial conditions. They found that changing the initial conditions and thereby the assembly history of a Milky Way-like galaxy is a significantly bigger effect than the intrinsic variability of the EAGLE model. They still found an intrinsic variation of the stellar mass at $z = 0$ of up to a factor of 2 for one set of initial conditions, and generally significant changes to the rotational support of the disc of the main galaxy at $z = 0$.

Lastly, to quantify the variance from stochastic modelling of star formation and feedback in the SWIFT–EAGLE model, Borrow et al. (2023) ran 16 realizations of a 25 Mpc^3 cosmological box. The SWIFT code is not deterministic anyway, as a result of its implementation of task-based parallelism that does not preserve the order or numerical operations. That is, if the simulation is run again on the same machine with the same number of tasks, it produces slightly different results. Therefore, they did not need to change the random number seed, because any initial deviation quickly changes the specific random number used for future operations. They found that the stellar mass even of well-resolved individual galaxies can vary by 25 per cent in the SWIFT–EAGLE model.

In this paper, we analyse the intrinsic variance of the Auriga galaxy formation model (Grand et al. 2017). Star formation histories and satellite mass functions of our set of seven cosmological zoom simulations of the same galaxy have already been shown in Grand et al. (2021) to understand and quantify resolution effects on the satellite population of a Milky Way-like galaxy. They found that the stochastic variability at fixed resolution for the Auriga model is significantly smaller than changes introduced by changing the numerical resolution, and that the satellite population is robust to stochastic variations as well. Here, we present a more general and detailed quantitative analysis of the same seven simulations with a focus on the central galaxy at $z = 0$.

2 SIMULATIONS

Our simulations are resimulations of the cosmological zoom-in simulation Au-6 of the Auriga project (Grand et al. 2017). The Auriga haloes are selected from the dark matter only simulation box of the EAGLE project (Schaye et al. 2015). They are chosen to have a halo mass of $10^{12} < R_{200,\mathrm{c}} < 2 \times 10^{12}\,\mathrm{M}_\odot$ at $z = 0$ and also fulfil a mild isolation criterion. Each halo's particles are traced back to the initial conditions to determine its Lagrangian region at high redshift. The Lagrangian region is resampled at higher resolution and augmented with an added safety buffer. The halo is then resimulated with the higher resolution in the Lagrangian region and the rest of the box is derefined to a much lower resolution. In this way, the zoom-in simulation focuses almost all resolution elements on a single halo and its environment, but keeps the large-scale structure, and in particular tidal gravitational forces acting on the halo, in place.

The simulations are run with the moving-mesh magnetohydrodynamics (MHD) code AREPO (Springel 2010; Pakmor et al. 2016; Weinberger, Springel & Pakmor 2020). It solves gravity with a combined tree and particle-mesh approach (Springel 2005; Springel et al. 2021). Gas is evolved on a moving Voronoi mesh with a second-order finite volume scheme (Pakmor et al. 2016). The Auriga galaxy formation model adds the physical processes that are relevant for the formation and evolution of galaxies. Specifically, it includes radiative cooling in the form of primordial and metal line cooling (Vogelsberger et al. 2013), an effective model for the interstellar medium and the formation of stars (Springel & Hernquist 2003), an effective model for galactic winds driven by stellar feedback, mass return from stars via stellar winds and supernovae, and a model for the seeding and growth of, as well as feedback from, supermassive black holes (Grand et al. 2017).

The main source of intrinsic randomness in the Auriga model is the formation of star particles and (galactic) wind particles. Both remove some or all gas from a cell (in the second case, removing the cell completely) to create a collisionless particle. They are both realized stochastically, where the creation of a star particle models star formation, and the wind particles are a model for the generation of galactic winds from stellar feedback. In each time-step, each star-forming cell has a non-zero probability to create a star particle or a wind particle (Grand et al. 2017). To realize this probability, a random number for each cell is drawn that determines whether the

Table 1. Global properties of our galaxy in all seven realizations at $z = 0$. The columns show from left to right the mass of the halo M_{200c}, i.e. the mass within a sphere around the potential minimum of the halo where the mean density is 200 times the critical density of the universe, the stellar mass of the main subhalo M_*, the stellar mass in the halo at a distance larger than 50 kpc $M_{*,R>50\,\mathrm{kpc}}$, the star formation rate in the last Gyr $\dot{M}_{1\,\mathrm{Gyr}}$, the maximum circular velocity $V_{c,max}$, the mass of the stellar disc M_{disc} and bulge M_{bulge}, the scale radius R_{disc} and height H_{disc} of the stellar disc, the radial σ_r and vertical σ_z velocity dispersion in the stellar disc at a radius of 8 kpc, and the total angular momentum of the stellar disc $|L_*|$. The last three rows show the mean value, variance, and the variance relative to the mean for all quantities over all seven realizations. Most properties vary by $\lesssim$10 per cent. Notably the stellar mass of the halo and the star formation rate at $z = 0$ vary by $\approx$30 per cent.

	Realizations at standard resolution (L4)											
Realization	M_{200c}	M_*	$M_{*,R>50\,\mathrm{kpc}}$	$\dot{M}_{1\,\mathrm{Gyr}}$	$V_{c,max}$	M_{disc}	M_{bulge}	R_{disc}	H_{disc}	σ_r	σ_z	$\lvert L_*\rvert$
	($10^{12}\,\mathrm{M}_\odot$)	($10^{10}\,\mathrm{M}_\odot$)	($10^{10}\,\mathrm{M}_\odot$)	($\mathrm{M}_\odot\,\mathrm{yr}^{-1}$)	($\mathrm{km\,s}^{-1}$)	($10^{10}\,\mathrm{M}_\odot$)	($10^{10}\,\mathrm{M}_\odot$)	(kpc)	(kpc)	($\mathrm{km\,s}^{-1}$)	($\mathrm{km\,s}^{-1}$)	($10^{18}\,\mathrm{M}_\odot\,\mathrm{kpc\,km\,s}^{-1}$)
0	1.05	5.66	0.39	3.7	213	0.42	4.81	3.9	0.85	49.6	40.5	6.5
1	1.04	5.47	0.78	1.6	211	0.42	4.13	4.1	0.88	50.3	40.7	5.7
2	1.03	5.09	0.43	2.1	200	0.42	4.18	5.2	0.93	46.5	38.2	6.8
3	1.03	5.32	0.46	1.6	203	0.42	4.33	4.8	0.88	45.0	37.8	6.9
4	1.05	5.39	0.72	3.3	206	0.44	4.22	4.7	0.89	47.7	39.8	6.4
5	1.04	5.42	0.41	2.4	206	0.43	4.54	4.7	0.87	46.6	38.5	6.9
6	1.05	5.36	0.46	2.0	209	0.39	4.45	4.0	0.91	46.8	40.5	5.9
Mean	1.04	5.39	0.52	2.4	207	0.42	4.38	4.5	0.89	47.5	39.4	6.5
σ	0.01	0.17	0.16	0.8	4.6	0.02	0.24	0.5	0.03	1.9	1.2	0.5
σ/mean (per cent)	1.0	3.2	30.6	33.6	2.2	4.0	5.5	10.7	3.1	3.9	3.1	7.2

cell creates either particle or not. Once created, the wind particles have a second set of random numbers drawn to determine their initial direction of motion before they recouple to the gas mesh.

Additionally, the feedback of the supermassive black hole in the low accretion rate mode (Grand et al. 2017) randomly places hot bubbles in the circumgalactic medium; however, in the regime of the Auriga galaxies, this type of feedback is usually subdominant (Grand et al. 2017; Irodotou et al. 2022).

In addition to randomness introduced by the physics model, we randomize the centre of the domain in every domain decomposition to decorrelate and therefore reduce force errors (Springel et al. 2021). The refinement also introduces randomness when deciding where to exactly introduce a new mesh-generating point when a cell is split (Springel 2010).

Importantly, the outcome of a simulation with the Auriga model (and with AREPO in general) is deterministic. Therefore, rerunning the same simulation again on the same machine with the same parallel set-up and libraries will lead to identical results. To test the intrinsic variance of the Auriga model in a controlled way, we thus redo one simulation seven times, with identical initial conditions, code, and model parameters, only changing the random number seed in AREPO for every resimulation. We call these resimulations different realizations of the same simulation. In this way, all seven realizations are equally valid outcomes of the Auriga model for the given initial conditions, and the differences between the different realizations directly allow us to quantify the intrinsic variance of the model. For the resimulations, we chose Au-6 of the Auriga project (Grand et al. 2017) at the standard resolution L4 (i.e. with a baryonic mass resolution of $5 \times 10^4\,\mathrm{M}_\odot$ and a dark matter mass resolution of $3 \times 10^5\,\mathrm{M}_\odot$). We resimulate Au-6 seven times, with identical initial conditions, code, and model parameters. We only change the random number seed in AREPO for every simulation.

3 GLOBAL PROPERTIES OF GALAXIES AND THEIR HALO

We show a summary of the global properties of the main galaxy and its halo in all seven realizations at $z = 0$ in Table 1. The total mass of the halo is robust to 1 per cent. The stellar mass of the central galaxy, and its decomposition into stellar bulge and disc components, change by 5 per cent or less between the realizations. To define the bulge and extended disc, we follow Marinacci, Pakmor & Springel (2014) and fit a Sérsic profile for the bulge and an exponential profile for the disc to the stellar surface density profile. Similarly, the size and height of the stellar disc, as well as its total angular momentum, vary only by $\approx$10 per cent and the stellar velocity dispersions at a radius of 8 kpc, as a proxy of the dynamical state of the stellar disc, only vary by less than 5 per cent between realizations. Here, we compute the size and height of the stellar disc by fitting exponentials to the radial and vertical profile of the stellar surface density. We have used this scale radius to compute the stellar mass of the disc.

Notably, the total stellar mass in the halo (at $50\,\mathrm{kpc} < R_{3D} < R_{200c}$) varies significantly. Here, we include satellite galaxies in the total stellar mass in the halo. The variability arises due to differences in the timing of satellite orbits between realizations which can result in satellites being outside the cut radius of 50 kpc in some realizations, and inside in others. The other notable variance is in the average star formation rate in the last Gyr, which varies by $\sim$30 per cent around the mean value between the realizations.

For a first visual impression of the differences between the galaxies formed in the different realizations, we show face-on and edge-on stellar light projections at $z = 0$ in Fig. 1. We compute these orientations from the angular momentum vector of the stellar disc. The directions of the total angular momentum vectors of the stars in the central galaxy deviate by less than 5° from the mean direction. The galaxies look overall very similar. They have a similar size and height, and are all dominated by young, blue stars in the outskirts. They also visually have similarly sized bulges. Interestingly, the internal structure of the stellar disc varies. In particular, R1 features a prominent non-axisymmetric bar-like structure, while R2 looks close to perfectly circular in the centre. The other realizations show mild non-axisymmetric structures somewhere in between R1 and R2. The formation of a bar in only one realization (R1) indicates that there is intrinsic stochasticity in the dynamical properties of this galactic disc, due to it being marginally bar-unstable (see e.g. Sellwood & Debattista 2009). In contrast, preliminary tests show that for systems that are highly bar-unstable (e.g. halo Au-18) bar formation is robust in different random realizations of the same halo (Fragkoudi et al., in preparation). Future detailed analysis of the

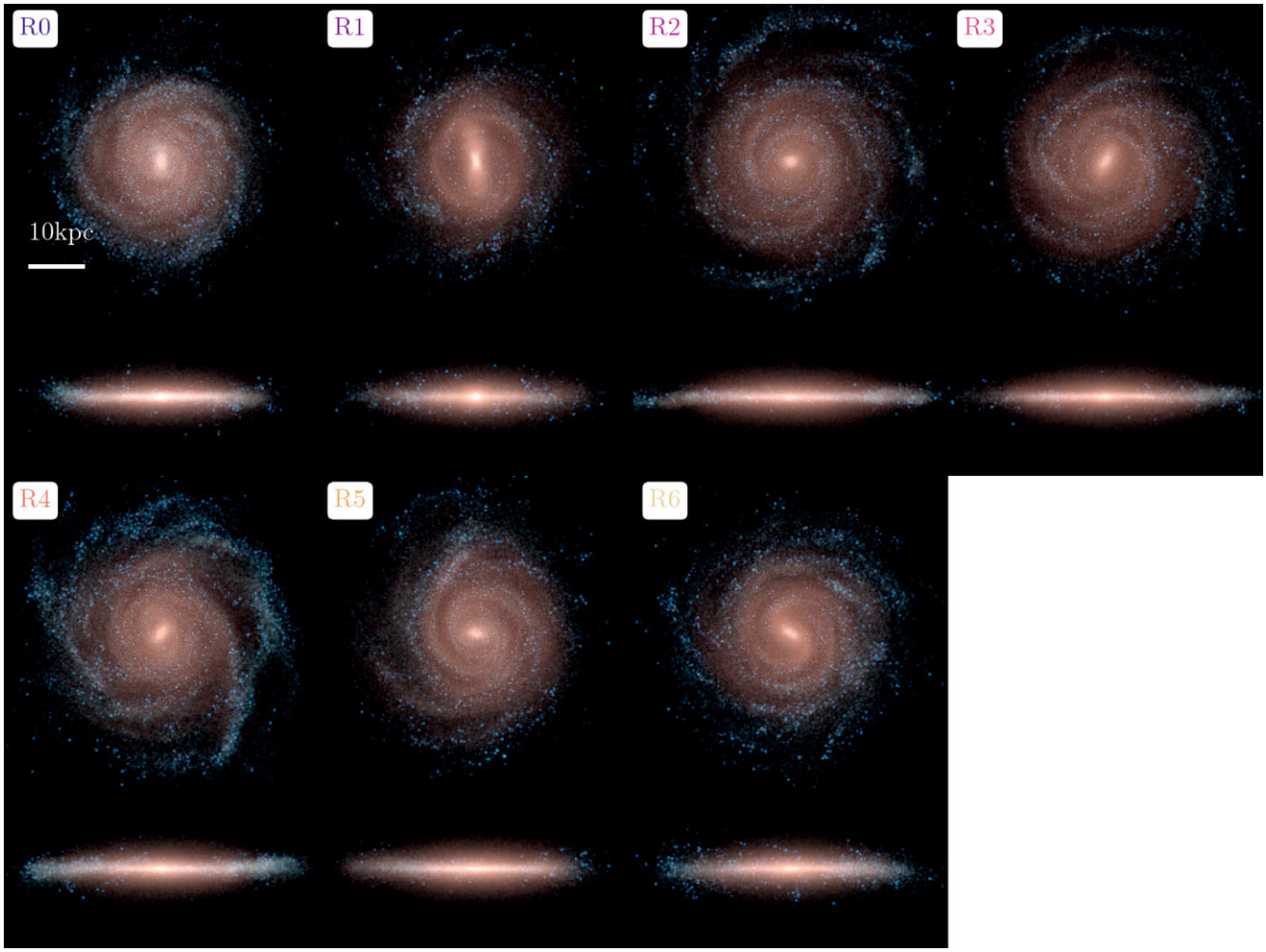

Figure 1. Stellar light projections of all seven realizations of Au-6 at resolution L4. All projections cover a 60 kpc × 60 kpc box for the face-on projections and a 60 kpc × 30 kpc for the edge-on projections. The galaxies all look very similar in colour and size. However, there is variation in their internal structure, in particular in the strength of the non-axisymmetric bar-like structure in the centre and their spiral features.

stochasticity in cosmological simulations will lend further insight into bar formation within the cosmological context.

All galaxies exhibit spiral structures, but they differ in detail. R6 features a clear inner two-armed spiral; the other galaxies show less regular spiral structures. Overall, the global properties of the stellar disc seem robust, but the detailed structural properties vary.

In Fig. 2, we show projections of the dark matter column density convolved with the local dark matter velocity dispersion rendered using a two-dimensional color map (Springel et al. 2005; Pakmor et al. 2023) at $z = 0$. The projections are computed along the z-axis of the simulation box, so that the orientation of the main halo and the positions of the satellites are directly comparable. The main halo looks very similar in all realizations with similar orientation and elongation. Moreover, the most massive satellite and many of the smaller satellites are present in all haloes, at similar positions. We conclude that the dark matter and satellite haloes, including their trajectories, are robustly modelled by our simulations. This holds at least until satellites fall deeply into the main halo, similar to simulations that only evolve dark matter and no baryons (see e.g. Springel et al. 2008). The deviations in the positions of smaller haloes relative to the main halo are caused by errors in the force calculation. Those are directly exposed here, because we add a random shift vector to the global domain at every domain decomposition to decorrelate force errors over time. This reduces the overall force error (Springel et al. 2021), and also leads to different force errors in the different realizations.

As a more quantitative measure of the matter distribution in the halo at $z = 0$, we show circular rotation curves of all realizations in Fig. 3 (top panel) and their deviation relative to the mean rotation curve of all realizations (bottom panel). The rotation curve directly measures the total enclosed mass at a given radius. Its overall shape is very similar between realizations. The radius where the circular rotation curve reaches its maximum varies only by a few kpc around 15 kpc. The value of the maximum varies only by a few per cent, from 195 to 215 km s^{-1}. In summary, the mass distribution in the halo at $z = 0$ is very similar for all realizations, and only varies slightly within the central galaxy.

To better quantify the difference in the stellar component of the main galaxy, we show the star formation histories of all galaxies in the top panel of Fig. 4, the relative deviation from the mean star formation rate in its middle panel, and the time evolution of the relative deviation of the stellar mass from the mean stellar mass in the bottom panel. Here, we include all star particles bound directly to the main halo at $z = 0$ (i.e. we exclude star particles bound to satellite

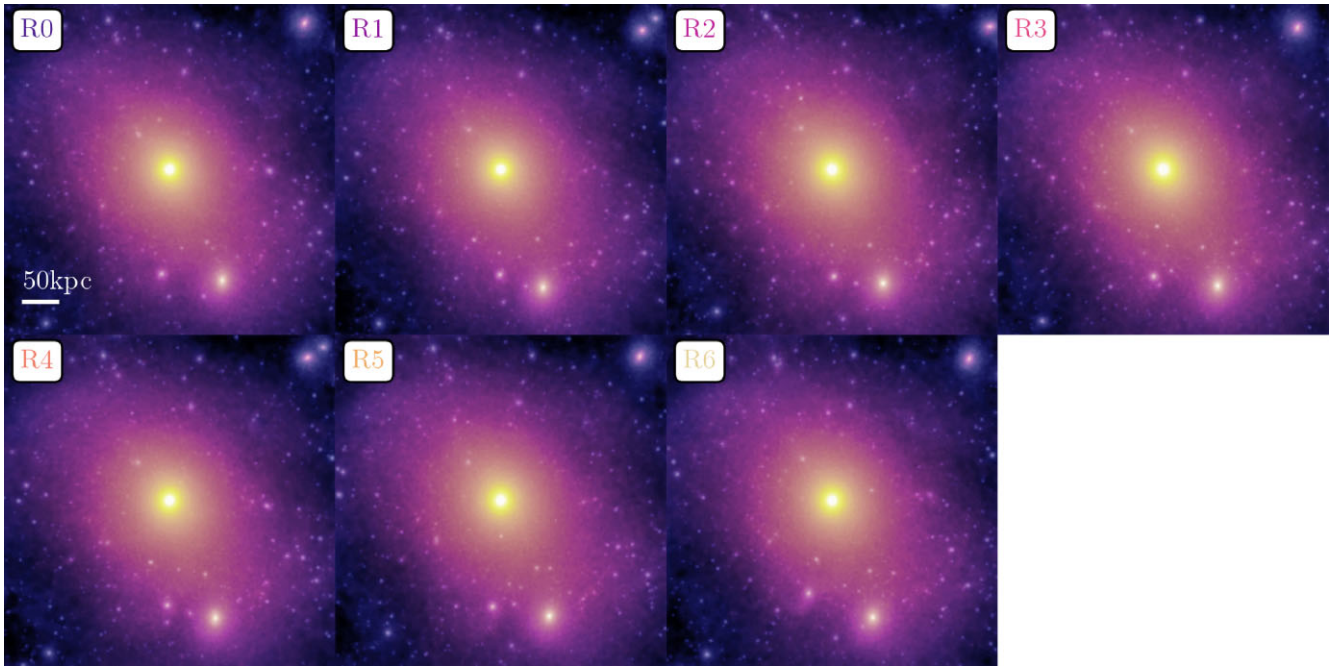

Figure 2. Projections of dark matter surface density and velocity dispersion with a two-dimensional color map (Springel, Frenk & White 2006). All projections cover a 500 kpc × 500 kpc box. The panels show all seven realizations of Au-6 at resolution L4. The properties of the main dark matter halo, as well as the positions of the most massive and many smaller satellites, are very similar.

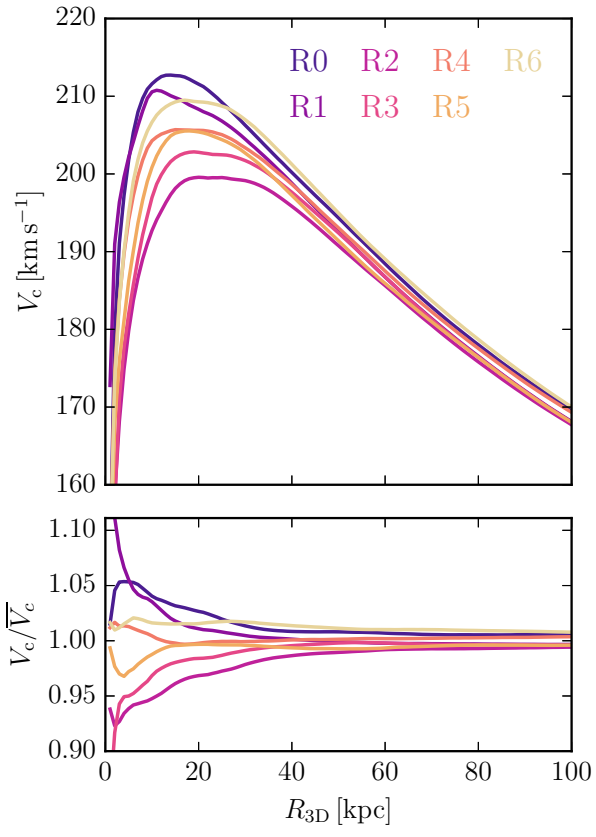

Figure 3. Circular velocity curves computed from the total enclosed mass of all seven realizations of Au-6 at resolution L4. The main difference is in the value of the peak or plateau around 20 kpc. At larger radii, circular velocity agrees on the per cent level.

galaxies). The star formation histories are essentially identical before $z = 2$ and very similar before $z = 1$. The initial deviation might be connected to either a significant merger just before $z = 2$ or the formation of a disc. After $z = 1$, they oscillate around a mean level of $\sim 10\,M_\odot\,yr^{-1}$ until $z \sim 0.4$ and then all decline steeply towards $z = 0$. At this time, they have dropped by more than a factor of 5 to a mean star formation rate of only $2\,M_\odot\,yr^{-1}$, with a significant variance of $1\,M_\odot\,yr^{-1}$. This variance is driven by differences in the gas accretion rate on the galaxy. Even though the relative difference at $z = 0$ is quite large, this has almost no effect on the total stellar mass of the galaxy, because it is dominated by stars formed at earlier times when the relative differences between the different simulations are much smaller. The total stellar mass only deviates by the level of a few per cent at all times.

4 PROPERTIES OF THE GALACTIC DISCS

Having established that the global properties of the main galaxy and its halo at $z = 0$ are very similar for the different realizations, we now focus in more detail on the internal properties and structure of the main galaxy. We first show profiles of the stellar surface density and their relative deviation from the mean profile over all realizations in the left panels of Fig. 5. Here, we conservatively include all star particles at a height $|z| < 30$ kpc in the main halo, though the profiles are completely dominated by the disc. The surface density profiles are all very similar, in normalization as well as in shape, and for both the bulge in the inner few kpc and the disc at larger radii.

To look at the full halo, we show cumulative stellar mass profiles of all realizations in the right panels of Fig. 5. Consistent with Table 1, we see that the total stellar mass in the halo is very similar. Notably, in R1, the stellar mass is more concentrated in the very centre of the galaxy. This central concentration is likely directly connected to the bar (Fragkoudi et al. 2025) that is prominently featured only in this realization (see Fig. 1).

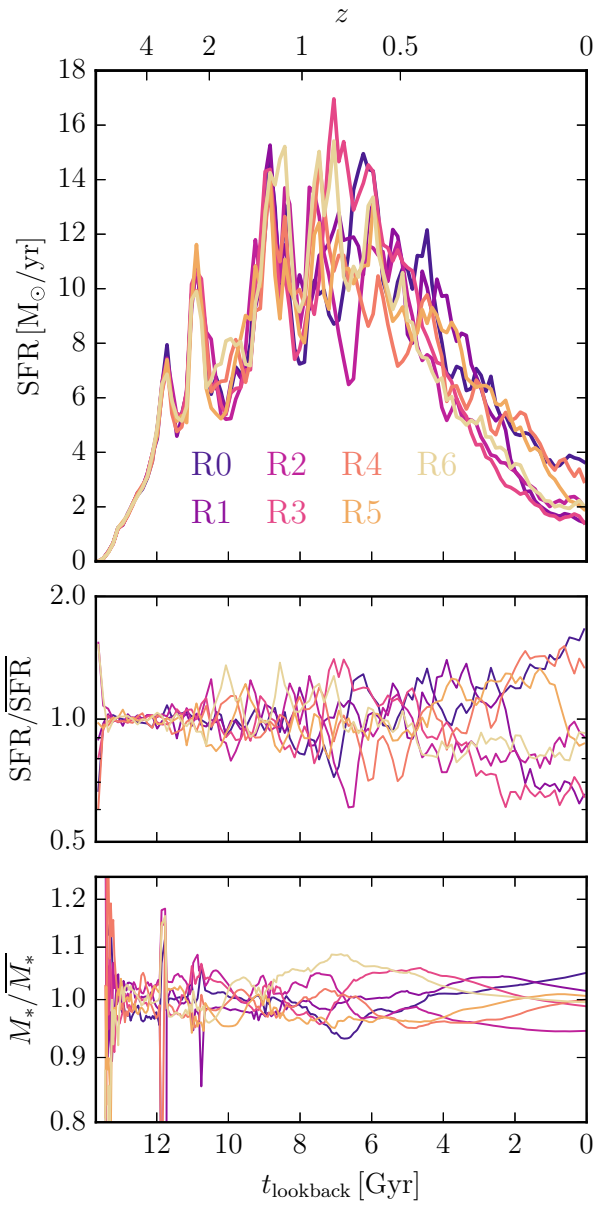

Figure 4. Star formation histories of all seven realizations of Au-6 at standard resolution L4 (top panel). They are essentially identical before $z = 1$. As the star formation rates decline towards $z = 0$, their relative differences (middle panel) increase, up to a deviation of ∼50 per cent relative to the mean. The total stellar mass deviates only by a few per cent over the whole evolution (bottom panel).

We show stellar metallicity profiles and their relative deviation from the mean profile in the left panels of Fig. 6. In the inner 15 kpc, the stellar metallicity profile only deviates by a few per cent. At larger radii, the deviation is significantly larger. In the very outskirts of the stellar disc at 30 kpc, the stellar metallicity varies from $0.5\,Z_\odot$ to $Z_\odot$. The deviation from the mean stellar metallicity profile (see lower left panel of Fig. 6) in the outskirts strongly correlates with the deviation from the mean stellar surface density profile (see lower left panel of Fig. 5). Higher stellar surface density leads to higher stellar metallicity and vice versa.

Having shown that the stellar discs are similar for the different realizations, we next look at gas metallicity profiles at $z = 0$ in the right panels of Fig. 6. The gas metallicity profiles have slightly larger scatter in the inner parts of the disc compared to the stellar metallicity profiles, and slightly smaller scatter in the outer parts. The scatter is still below 20 per cent at all radii.

We then look at the magnetic fields in the mid-plane of the disc at $z = 0$ as a proxy to compare how similar the gas discs are. Magnetic fields affect the gas dynamics and are an important tracer of the state of the gas in both the disc (Pakmor, Marinacci & Springel 2014; Pakmor et al. 2017, 2018, 2024; Whittingham et al. 2021, 2023) and the circumgalactic medium (Pakmor et al. 2020; van de Voort et al. 2021). Note that this comparison is only really meaningful because the stellar discs, which dominate the potential in the galaxy and therefore the gas dynamics in the galaxy as well, are so similar.

We show the magnetic field strength profile in the disc in Fig. 7 (left panels) and in the full halo (right panels) at $z = 0$. The magnetic field strength profiles in the discs are similar. At a given radius, the magnetic field strength deviates by less than a factor of 2 around the mean profile. R1 is again an interesting outlier, which has a significantly stronger magnetic field in the very centre of the galaxy. This is likely a result of the higher stellar mass and therefore deeper potential in the very centre of the galaxy, and possibly also connected to the presence of a bar as discussed above.

The magnetic field strength in the halo outside the galaxy, i.e. at radii larger than $R_{3D} \gtrsim 30$ kpc, also agrees well for the different realizations. Most of the realizations deviate less than 20 per cent from the mean magnetic field strength profile. Notably, R4 has a slightly lower magnetic field strength in the halo, but approaches the mean profile at the edge of the halo.

In the Auriga galaxies, magnetic fields are quickly amplified when the galaxy first forms at high redshift. This turbulent dynamo saturates before a stable gas disc forms around $z = 2$ (Pakmor et al. 2017, 2024). The rotation in the gas disc then orders and further amplifies the magnetic field. At $z = 0$, it is typically dominated by a large-scale ordered field (Pakmor et al. 2018, 2024). Therefore, the structure of the magnetic field at $z = 0$ can also provide important diagnostics for the evolution of the galaxy and its gas disc.

We show slices of the magnetic field components in cylindrical coordinates in the disc at $z = 0$ for all realizations in Fig. 8. As a first impression, we see that all three components (azimuthal magnetic field in the top row, radial magnetic field in the middle row, and vertical magnetic field in the bottom row) show qualitatively similar structures in all realizations. All galaxies feature large-scale ordered azimuthal magnetic fields that are about three times stronger than the radial and vertical magnetic fields.

Field reversals in the azimuthal field are rare; the galaxies only have either zero or one field reversals. The sign of the ordered field is not a robust outcome, however. This is not surprising, as the equations of ideal MHD are agnostic about the sign of the magnetic field. Therefore, either ordered configuration is physically indistinguishable.

The vertical magnetic fields (shown in the bottom row of Fig. 8), in contrast, are not ordered on large scales. They all show signs of being wound up from an initial, chaotic, small-scale field. This leads to a field that is ordered along the azimuth with many field reversals. Its strength is also similar for all galaxies.

The radial magnetic field (middle row of Fig. 8) has an intermediate structure. It shows some hints of large-scale ordering, but still has most of the small-scale structure and many field reversals of the vertical field. Its strength is also similar for all realizations. One notable outlier is again R1, which has a significantly stronger radial field in the centre of the galaxy, and shows the dipolar pattern typically associated with bars.

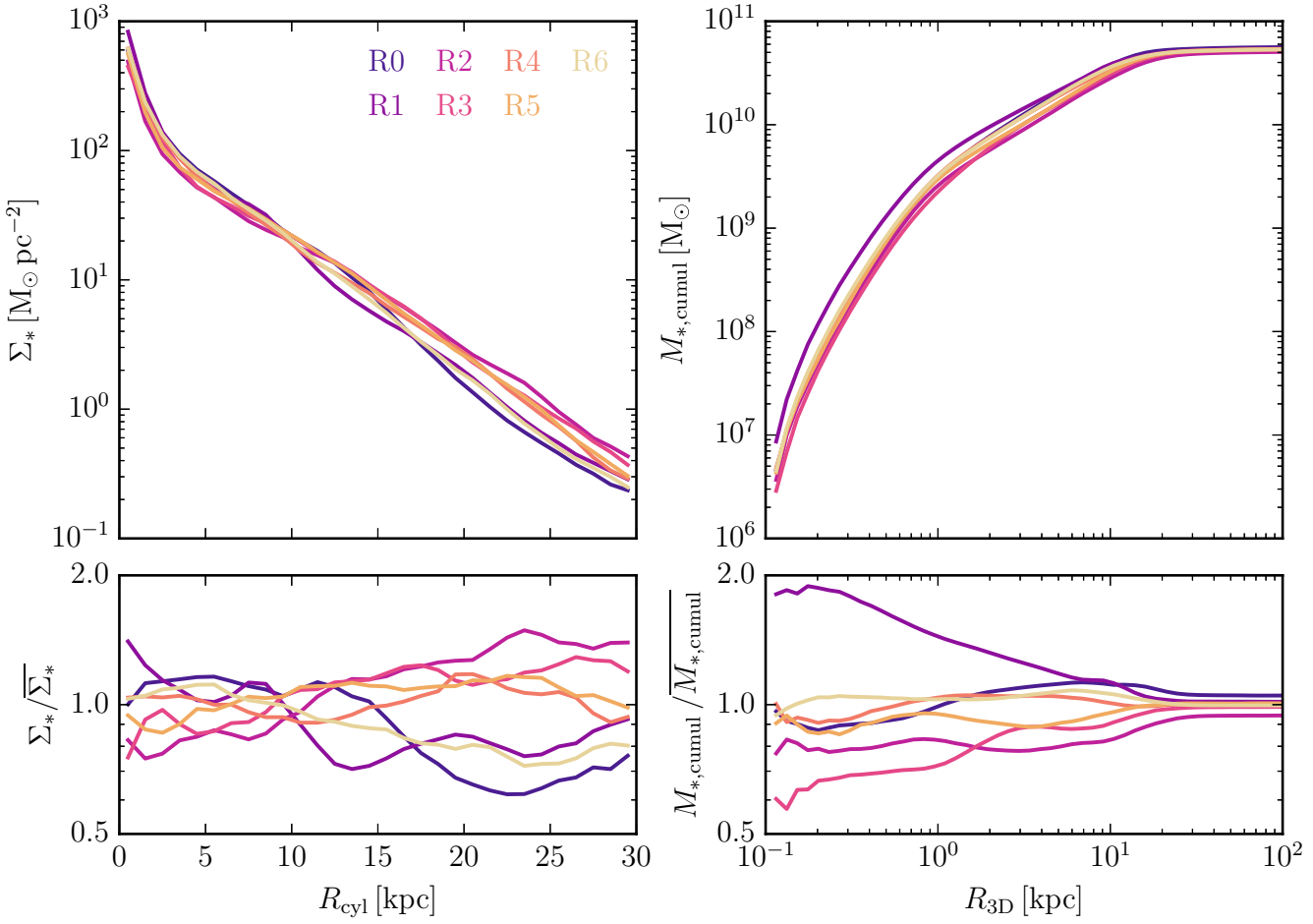

Figure 5. Stellar mass surface density (left panel) and cumulative stellar mass (right panel) for all seven realizations of Au-6 at resolution L4. The surface density profiles are very similar in the inner part as well as in their slope in the disc. The total stellar mass in the full halo is very similar as well, but the distribution in the halo varies somewhat between realizations.

5 SATELLITE GALAXIES

In addition to the central galaxy, a cosmological zoom-in simulation also contains a number of smaller galaxies, some of them satellites of the main galaxy. The latter are interesting in and of themselves and as a diagnostic for the galaxy evolution model (Simpson et al. 2018; Grand et al. 2021). They also interact with their central host galaxy. They shape its stellar halo and create stellar streams (Monachesi et al. 2016, 2019; Riley et al. 2025; Shipp et al. 2025; Vera-Casanova. et al. 2025), they also influence the disc of the central galaxy, and they contribute to substructures in the disc and inner halo (Gómez et al. 2016, 2017; Gargiulo et al. 2019; Simpson et al. 2019). Therefore, it is crucial to understand how similar the satellites are between realizations when they fall into the halo, to determine how robust their evolution is until their possible disruption.

Fig. 9 shows the satellite mass function (left panel), which shows the total mass of all satellites at $z = 0$, and the satellite luminosity function (right panel), which shows the V-band luminosity of all satellites at $z = 0$. As discussed in detail in Grand et al. (2021), both show very good agreement between the different realizations, and we conclude that they are robust outcomes of our simulations.

In addition to looking at satellite galaxies that survive until $z = 0$, it is interesting to compare satellites that are destroyed. As an example, we show in Fig. 10 the evolution of one satellite that is eventually destroyed. As a representative case, we select the third most massive (by stellar mass) satellite among those disrupted before $z = 0$ in R0. We then match it to the other realizations by tracing back the 100 most bound dark matter particles of each satellite at the time it reaches its peak mass to the initial conditions (see also Riley et al. 2025). We then compute the centre of mass of these particles, and find the satellite that most closely matches the centre of our reference satellite selected from R0.

Fig. 10 shows the time evolution of the distance of this satellite to the centre of the main galaxy (left panel), the time evolution of the total mass of the satellite (middle panel), and the time evolution of the stellar mass of the satellite (right panel). The initial trajectory of the satellite when it falls into the main halo until it reaches its first closest encounter (pericentre) and its total mass and stellar mass at the time of infall are essentially identical. The trajectories of the satellite in the different realizations start to deviate slightly after their second apocentre passage, and spread more and more with every further orbit. The periods of the orbit of the satellite remain similar in the different realizations, but they deviate enough to quickly change the phase of the orbit. The realizations of the same halo will potentially allow us to understand which properties of the parent halo are the main source of the differences in the satellite trajectories.

The time when the satellite is eventually destroyed, i.e. when it is not found by subfind anymore as a bound object, varies from $t_{\rm lookback} = 3$ to 2 Gyr between the different realizations, with one notable outlier (R3). In this realization, the satellite survives more

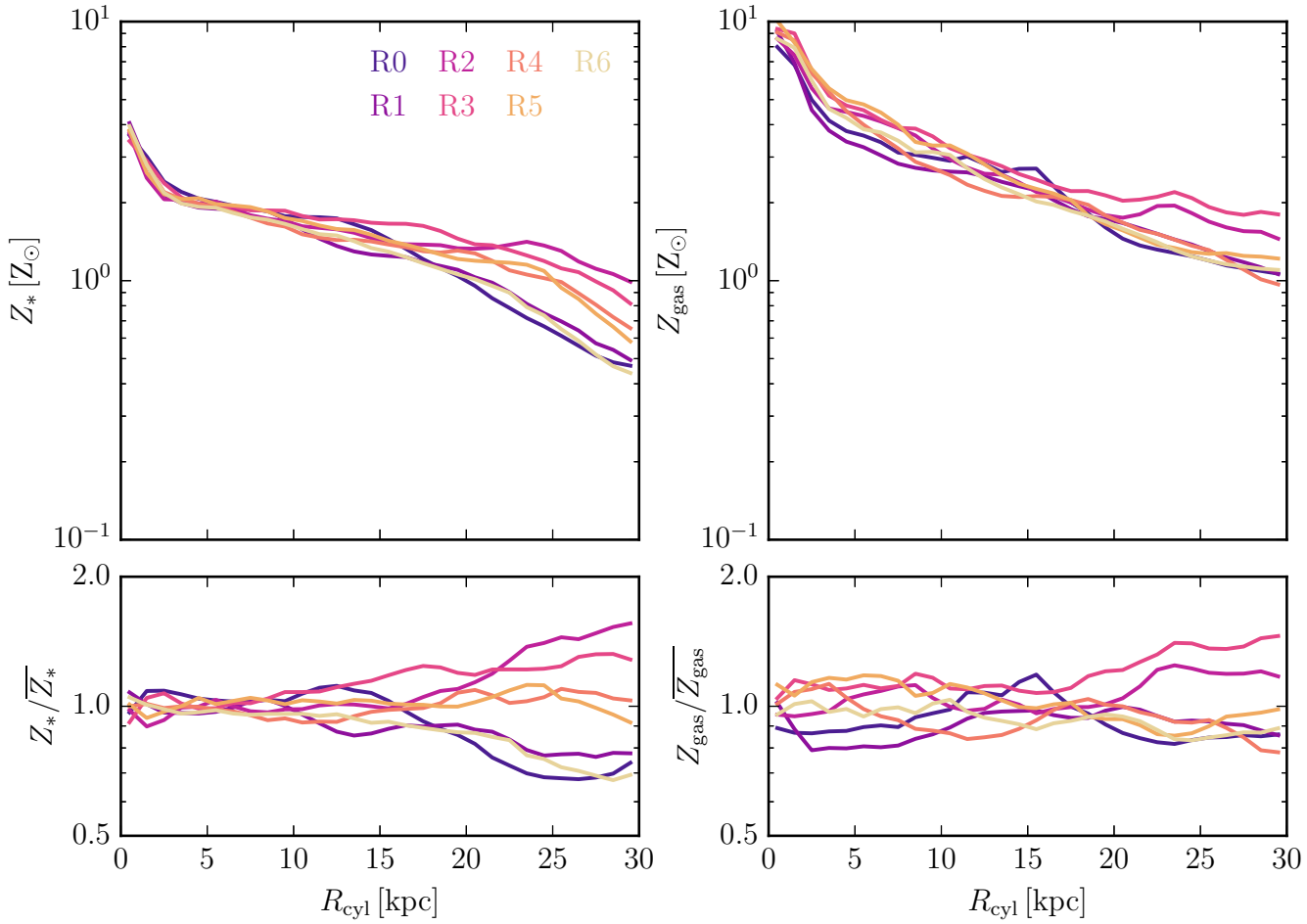

Figure 6. Metallicity profiles of stars (left panels) and gas (right panels) in the disc at $z = 0$ in cylindrical coordinates for all seven realizations of Au-6 at the standard resolution L4. In the inner 15 kpc, the stellar metallicity profile is essentially identical; at larger radii, it varies from $0.5\,Z_\odot$ to $Z_\odot$. The gas metallicity shows slightly larger scatter in the inner parts and slightly less scatter in the outer parts, compared to the stellar metallicity profiles.

than 2 Gyr longer than in the realization where it survives for the second longest time. The total mass and stellar mass of the satellite both initially evolve very similarly between the different realizations, which means that mass stripping is robust for a fixed numerical resolution. After several orbits, at $t_{\rm lookback} \approx 5$ Gyr the realization (R3) in which the satellite survives significantly longer starts to diverge, as the satellite is stripped less quickly than in the other realizations. This is possibly a consequence of a slightly larger first apocentre distance, but more work will be required to understand this difference in detail. The other realizations evolve very similarly all the way to the destruction of the satellite.

6 INTRINSIC VARIANCE AND NUMERICAL RESOLUTION

Having quantified the intrinsic variance of the Auriga model at fixed numerical resolution, an obvious next step is to extend this comparison to simulations with different numerical resolutions. In Fig. 11, we compare two sets of simulations with seven realizations each. We use the realizations discussed in this paper at the standard resolution of Auriga (L4), and a set of simulations with eight times worse mass resolution (L5) for all mass components, i.e. for gas, stars, and dark matter. We compare star formation histories (left panels of Fig. 11) and profiles of the stellar mass surface density at $z = 0$ (right panels of Fig. 11). The bands show interpolated 16th and 84th percentiles. We immediately see that for the first 10 Gyr of cosmic evolution, the star formation rate is systematically lower by ≈20 per cent in the simulations with worse mass resolution than in the standard resolution simulations. The difference is much larger than the intrinsic variability at fixed resolution. This difference is consistent with previous results for the Auriga model (Grand et al. 2017, 2021) and similarly the IllustrisTNG model (Pillepich et al. 2018). In the last few Gyr, when the star formation rate drops significantly in all simulations and the relative fractional difference between simulations at the same resolution increases (see also Fig. 4), the distributions overlap. However, the mean is still shifted systematically to lower star formation rates at lower resolution.

Moreover, because the star formation rate is lower over the whole evolution of the galaxies in the lower resolution simulations, their stellar mass at $z = 0$ is also systematically lower. Looking at the stellar surface density profiles at $z = 0$ (right panels of Fig. 11) we can see that the deficit of stellar mass in the lower resolution simulations is distributed over the full galaxy and not limited to either the central bulge or the extended disc. The systematically different stellar surface density profiles also imply that the dynamical state of the stellar disc is different, which modifies the conditions for internal processes of the disc, for example, for the formation of a bar (Fragkoudi et al. 2021, 2025). As a result, it becomes difficult to disentangle

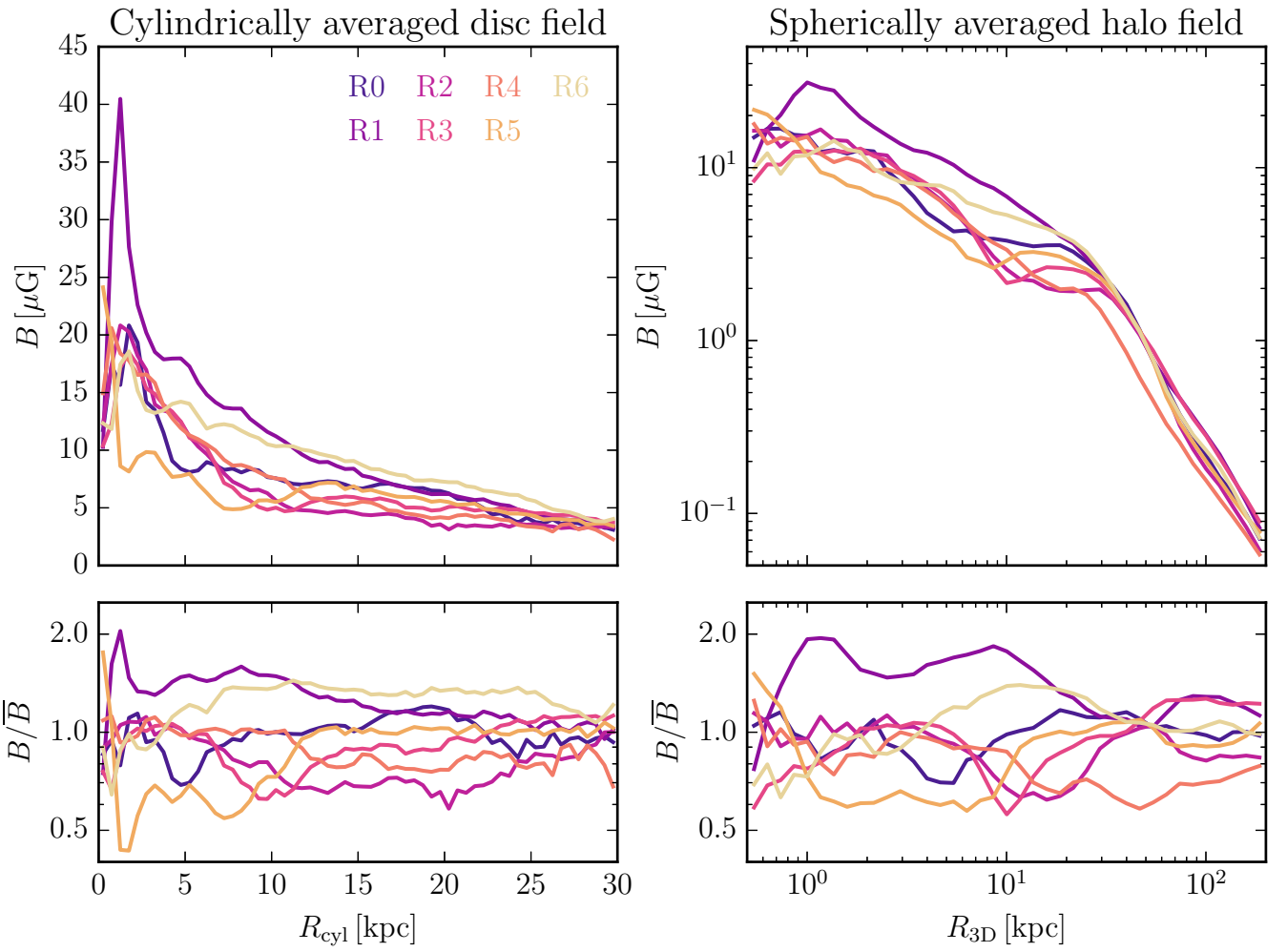

Figure 7. Radial profiles of the strength of the magnetic field at $z = 0$ for all seven realizations of Au-6 at resolution L4. The left panel shows the profile in the disc cylindrical coordinates computed from a root-mean-square average of all cells with a height $z < 100$ pc. The right panel shows the spherically averaged profile out to the virial radius of the halo. The magnetic field strength profiles are consistent within a factor of 2, both in the disc and in the halo.

genuine resolution effects on specific physical processes, such as bar formation, from the broader structural differences introduced by resolution. This limits the interpretability of resolution studies not only when they focus on the disc but also for all other properties of the satellites and halo that might be affected by the central disc galaxy and its feedback processes.

We see a similar effect for the satellite galaxy in Fig. 12 (the same that is shown in Fig. 10), where we show the time evolution of the stellar mass of a satellite matched between all realizations of all simulations of both resolution levels. We see that the satellite galaxy has a systematically lower stellar mass at all times before it falls into the main galaxy in the lower resolution simulations (L5). This systematic difference essentially disappears when the satellite galaxy starts to get stripped and loses stellar mass. The satellite tends to be destroyed marginally faster in the lower resolution simulation. For most other satellites (not shown), however, their destruction time is not significantly different for simulations at different resolutions. The different resolution dependence of the destruction time might depend on details of the orbit of the satellite and the mass and other properties of the stellar disc of the central galaxy that change as well. Even if the satellite galaxy gets destroyed at the same time in different resolution simulations, it will still have contributed less stellar mass to the halo in the lower resolution simulations, biasing the stellar halo systematically in the lower resolution simulation in a similar way as the central galaxy. The maximum stellar mass of the satellites in the lower resolution (L5) runs is lower by 20 per cent compared to the standard resolution (L4) runs. This ratio is the same as the ratio of the stellar masses of the central galaxies at $z = 0$ for the different resolutions.

Finally, we summarize the same global properties of the main galaxy and its halo at $z = 0$ shown in Table 1 for the standard (L4) resolution realizations, also for the lower resolution (L5) realizations in Table 2. Comparing the mean and variance of the stellar properties of the $z = 0$ stellar disc of the standard resolution realizations (L4) and lower resolution realizations (L5), we see that for most stellar properties (stellar mass, disc mass, bulge mass, and disc height) the differences introduced by changing the resolution are significantly larger than the intrinsic variance of the model at fixed resolution. Notably, there are hints that the intrinsic variance decreases with higher resolution. This is probably a result of the reduced impact of each random number in the higher resolution simulations. The latter has more star-forming cells in the same galaxy. It draws an independent random number for each of those cells to determine if it creates a star particle or a wind particle, and each star particle

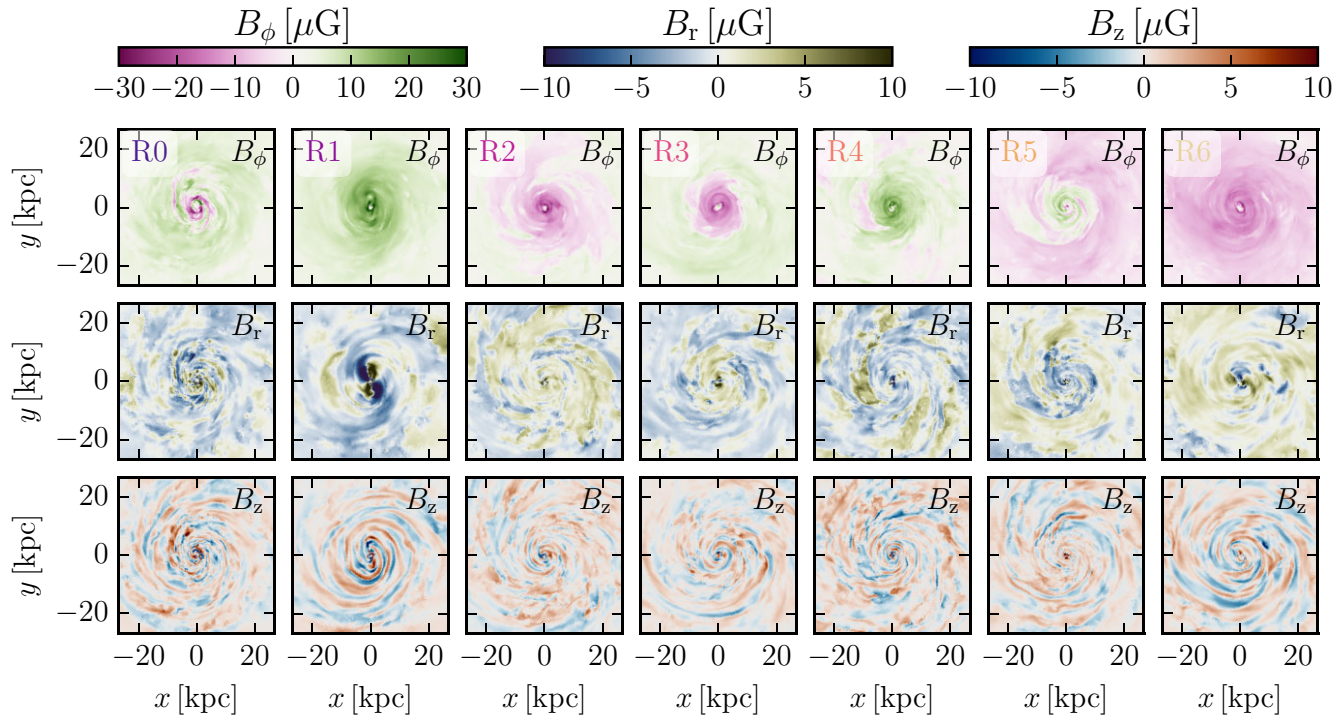

Figure 8. Slices of the different components of the magnetic field in cylindrical coordinates at $z = 0$ for all seven realizations of Au-6 at resolution L4. The basic magnetic field properties are remarkably similar for all galaxies. They are dominated by an ordered azimuthal field and show a slightly more chaotic radial field, and a much less ordered vertical field with many field reversals. The detailed structure, in particular the number of field reversals in the azimuthal field, seems stochastic.

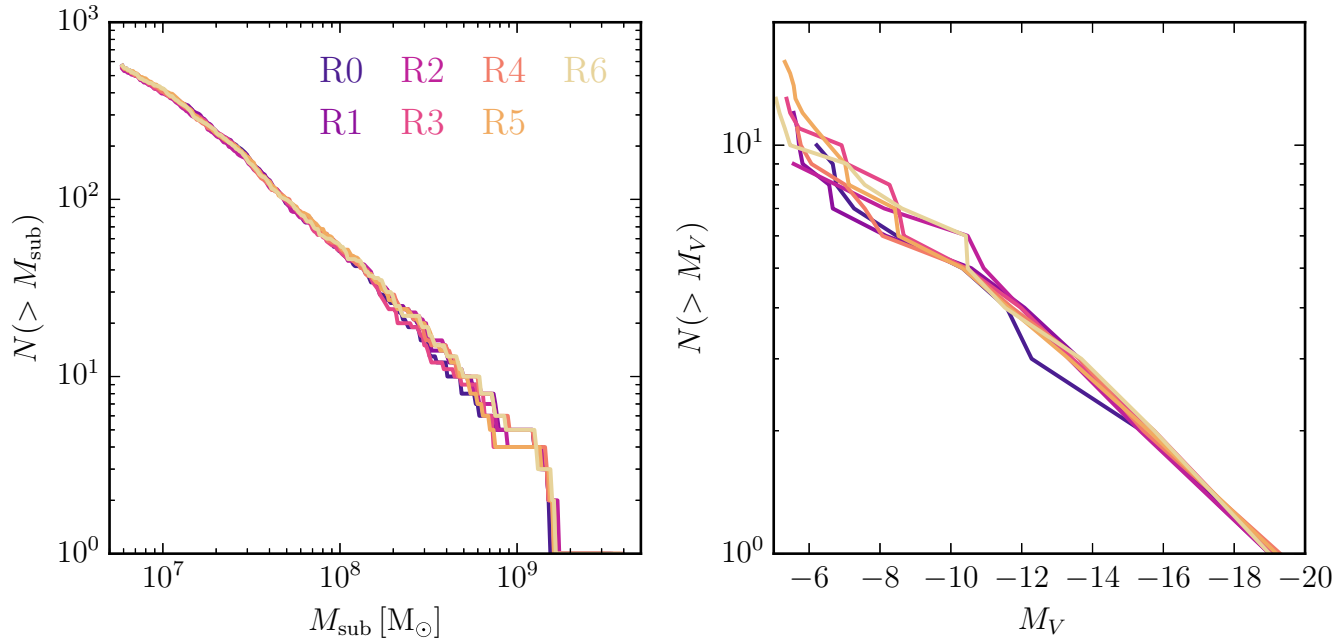

Figure 9. Satellite total mass function (left panel) and V-band luminosity function (right panel) at $z = 0$ for all seven realizations of Au-6 at resolution L4. The mass functions are essentially identical. The luminosity function only shows significant scatter for $M_V > -10$, with a single outlier at $M_V = -12$ for R0.

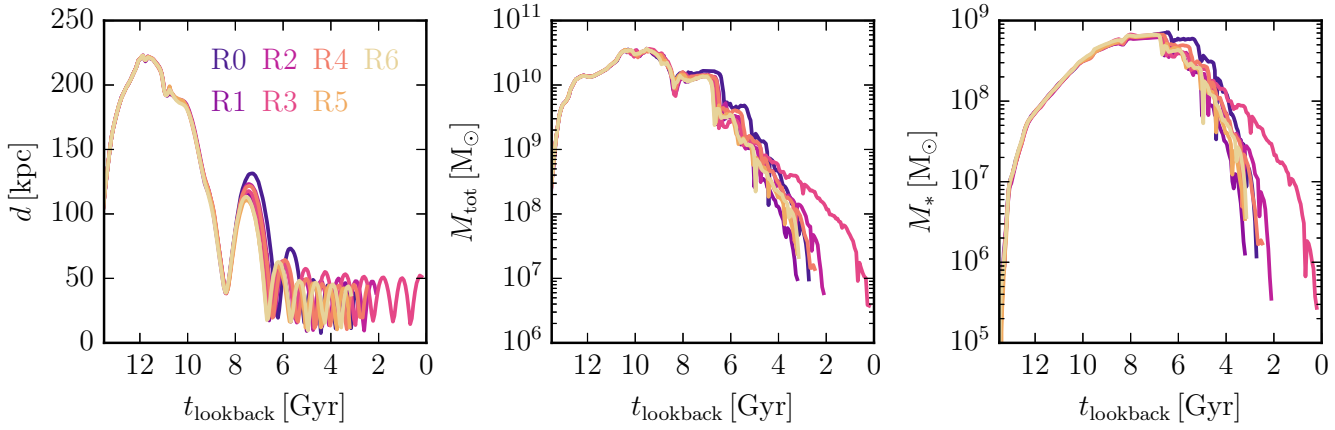

Figure 10. Trajectories of one relatively massive satellite that is destroyed before $z = 0$ for all seven realizations of Au-6 at resolution L4. The panels show the time evolution of the distance to the centre of the galaxy (left panel), total bound mass (middle panel), and total bound stellar mass (right panel). The satellite falls in with essentially identical properties. The longer it orbits the main galaxy, the more its properties deviate between the realizations.

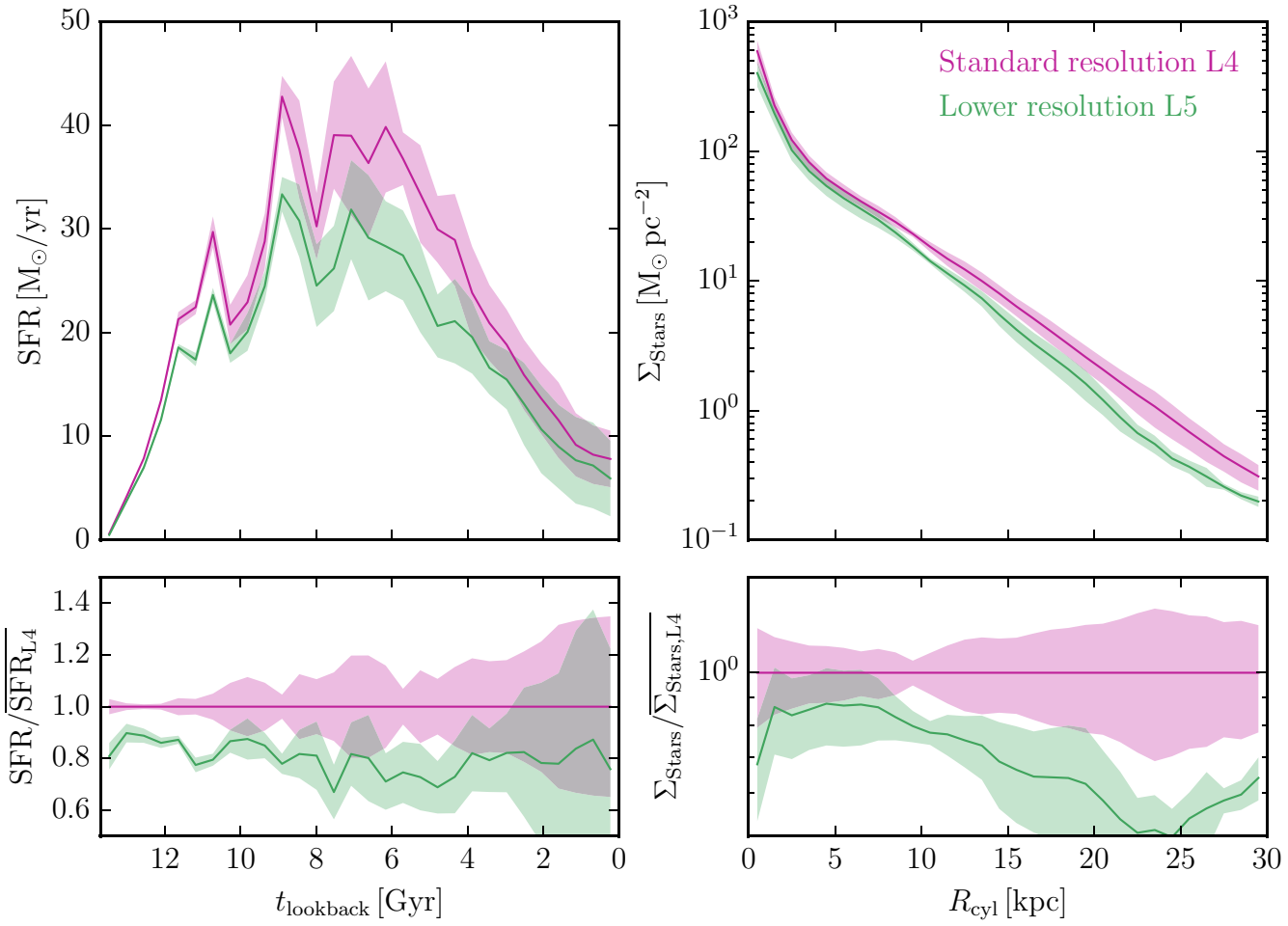

Figure 11. Star formation histories (top left panel) and stellar mass surface density profiles (top right panel) of the main galaxy for all seven realizations of Au-6 at standard resolution L4 and eight times lower resolution L5 . The shaded regions show interpolated 16th and 84th percentile bands around the mean profile (solid lines). The bottom panels show the same relative to the mean of all simulations at L4. The differences between the two resolution levels in all quantities are significantly larger than the variations between realizations at fixed resolution.

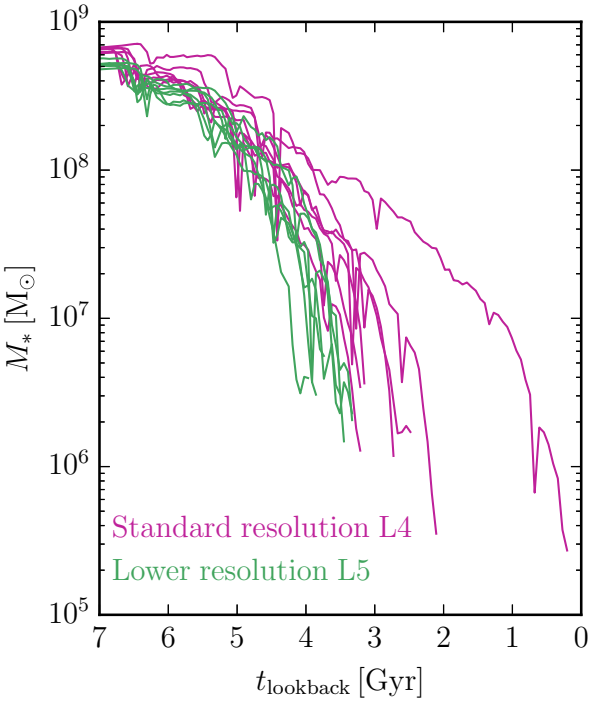

Figure 12. Time evolution of the stellar mass of one matched satellite galaxy of the main galaxy for all seven realizations of Au-6 at the standard resolution L4 (the same as in the right panel of Fig. 10) and eight times lower resolution L5. Similar to the main galaxy, the peak stellar mass of the satellite galaxy is lower for the lower resolution simulation. The satellite is destroyed slightly earlier on average in the lower resolution simulation.

and wind particle is less massive. Therefore, the importance of each random number is lower in the higher resolution simulation, and extreme outliers become rarer.

The IllustrisTNG model also shows a reduction of variability at better numerical resolution when comparing pairs of Milky Way-like galaxies in different realizations (Genel et al. 2019). However, this reduction of variability mostly disappears for lower mass galaxies. Moreover, Genel et al. (2019) demonstrate that for sufficiently high numerical resolution, the variability in the IllustrisTNG model for these low-mass galaxies is not primarily driven by random numbers in the subgrid model.

7 SUMMARY AND DISCUSSION

We have quantified the intrinsic variability of the Auriga model as applied to a cosmological zoom-in simulation of a Milky Way-like galaxy. We showed in Figs 2 and 3 that the dark matter structures, including the shape and total mass profile of the main halo and the positions of the satellites at $z = 0$, are robust, with relative deviations from the mean only on the per cent level.

Moreover, we showed that the global properties of the stellar disc of the main galaxy at $z = 0$, including its total mass and star formation history (see Fig. 4) and its stellar surface density profile (see Fig. 5), are robust, with relative deviations from the mean profile smaller than ≈30 per cent. Variations in global quantities are even smaller, i.e. the total stellar mass of the central galaxy, of its bulge and extended disc, as well as the stellar mass of satellite galaxies, deviate by only ≈5 per cent. Similarly, the strength (see Fig. 7) and structure (see Fig. 8) of the magnetic field in the disc and circumgalactic medium are a robust outcome of the simulation and deviate by less than a factor of 2 locally. Therefore, they are useful properties for comparison to observations. We also showed that the satellite population of the main halo at $z = 0$ (see Fig. 9) and the properties and evolution of individual satellites and their stripping and potential eventual destruction are robust in the Auriga model, at least until first pericentre passage (see Fig. 10).

All properties of the central galaxy of all realizations are much more similar than the initial set of 30 galaxies of the Auriga project (Grand et al. 2017) that are all in relatively isolated Milky Way-mass haloes. Thus, their formation histories seem to robustly determine their global properties, much more than the intrinsic variability of the Auriga model and the numerical schemes. This strengthens comparisons between different haloes of the Auriga project with the aim of connecting physical properties of galaxies to their formation history. It will also allow us to better understand how different

Table 2. Global properties of our galaxy in all seven realizations at $z = 0$ for the lower resolution simulations (L5). The columns show from left to right the mass of the halo M_{200c}, the stellar mass of the main subhalo M_*, the stellar mass in the halo at a distances larger than 50 kpc $M_{*,R>50\,\rm kpc}$, the star formation rate in the last Gyr $\dot{M}_{1\,\rm Gyr}$, the maximum circular velocity $V_{c,\rm max}$, the mass of the stellar disc $M_{\rm disc}$ and bulge $M_{\rm bulge}$, the scale radius $R_{\rm disc}$ and height $H_{\rm disc}$ of the stellar disc, the radial σ_r and vertical σ_z velocity dispersion in the stellar disc at a radius of 8 kpc, and the total angular momentum of the stellar disc $|L_*|$. The last three rows below show the mean value, variance, and the variance relative to the mean for all quantities over all seven realizations. The lowest row shows the relative difference of the mean to the mean of the simulations at the standard resolution (L4) shown in Table 1. Resolution in particular changes stellar masses significantly more than the intrinsic variation.

Realization	Realizations at lower resolution (L5)											
	M_{200c} (10^{12} M$_\odot$)	M_* (10^{10} M$_\odot$)	$M_{*,R>50\,\rm kpc}$ (10^{10} M$_\odot$)	$\dot{M}_{1\,\rm Gyr}$ (M$_\odot$ yr^{-1})	$V_{c,\rm max}$ (km s^{-1})	$M_{\rm disc}$ (10^{10} M$_\odot$)	$M_{\rm bulge}$ (10^{10} M$_\odot$)	$R_{\rm disc}$ (kpc)	$H_{\rm disc}$ (kpc)	σ_r (km s^{-1})	σ_z (km s^{-1})	$\lvert L_*\rvert$ (10^{18} M$_\odot$ kpc km s^{-1})
0	1.04	4.37	0.22	1.5	204	0.35	3.78	3.7	1.10	46.8	39.0	4.4
1	1.04	4.07	0.29	0.3	198	0.35	3.40	4.0	1.04	43.5	37.1	4.0
2	1.03	4.17	0.31	2.9	204	0.35	3.49	3.7	1.14	50.0	40.1	4.0
3	1.03	4.74	0.60	3.2	203	0.35	3.74	4.0	1.00	46.5	38.5	4.7
4	1.05	4.47	0.27	1.7	204	0.36	3.76	3.6	1.04	45.6	38.7	4.3
5	1.02	4.16	0.24	3.3	200	0.37	3.57	4.4	1.26	47.5	41.7	4.6
6	1.03	3.77	0.29	1.0	195	0.37	3.13	4.9	1.41	44.1	37.8	4.1
Mean	1.03	4.25	0.32	2.0	201	0.36	3.55	4.0	1.14	46.3	39.0	4.3
σ	0.01	0.31	0.13	1.2	3.7	0.01	0.24	0.5	0.15	2.2	1.5	0.3
σ/mean (per cent)	0.9	7.3	40.6	58.3	1.8	2.7	6.7	11.4	12.8	4.7	3.9	6.6
(mean − mean$_{\rm L4}$)/(mean$_{\rm L4}$) (per cent)	−0.8	−21.1	−39.4	−17.5	−2.7	−14.8	−18.8	−9.5	28.6	−2.6	−1.1	−33.6

physical properties of galaxies are correlated and caused by each other in our set of realizations that all have the same formation history.

Finally, we showed in Figs 11 and 12 that changing the numerical resolution of the simulation by a factor of 8 leads to significant systematic changes, which are much bigger than the intrinsic variability of the Auriga model at fixed resolution. The small intrinsic variance of the Auriga model makes it attractive to study physical model variations at fixed resolution (see e.g. Pakmor et al. 2017; Buck et al. 2020; van de Voort et al. 2021; Rodríguez Montero et al. 2024). However, the systematic changes to the galaxy properties with changing numerical resolution not only limits proper resolution studies, but also limits going to higher resolution without recalibrating a model.

Recent studies looking into the intrinsic variability of galaxy formation models have shown that it is important to understand the robustness of a model to interpret its results, and that the robustness is significantly different for different models (Genel et al. 2019; Keller et al. 2019; Davies et al. 2021; Borrow et al. 2023). A detailed quantitative comparison between the intrinsic variability of different models is hard because most published work limits quantitative discussions to the total stellar mass.

The four different feedback models discussed in Keller et al. (2019) show significant differences. They focus on the evolution of stellar mass and show that their 'superbubble' feedback has the largest variance in stellar mass of 10 per cent at $z = 2$ over 128 realizations and of 20 per cent between a pair of simulations evolved further to $z = 0.8$. For this model, they also find differences in the stellar surface density at $z = 0.8$ of almost an order of magnitude. This level of variance is significantly larger than for the Auriga model. Their other feedback models have comparable variance at $z = 2$ and lower variance at $z = 0.8$, but at the cost of inefficient feedback that is essentially consistent with no feedback.

The comparison of a set of large volume simulations with the IllustrisTNG model (Genel et al. 2019) showed that massive galaxies can end up with completely different morphologies. This is a result of the very stochastic radio-mode active galactic nucleus (AGN) feedback model of IllustrisTNG. The Auriga model, which is very similar to the IllustrisTNG model in terms of stellar feedback, features a radio-mode AGN feedback model that is much more gentle and less stochastic (Grand et al. 2017). The IllustrisTNG simulations also show roughly 5 per cent variance in the value of the maximum of the circular velocity curve, averaged over about 100 Milky Way-like galaxies. This is roughly consistent with our results for the Auriga model. The stellar mass of matched Milky Way-like galaxies between the IllustrisTNG boxes varies by 10 per cent at $z = 0$ for the highest resolution box with roughly comparable mass resolution to the standard Auriga (L4) resolution, slightly larger than the variance ($\lesssim$5 per cent) we find for our single galaxy.

Similar studies with the EAGLE model (Davies et al. 2021) and the SWIFT–EAGLE model (Borrow et al. 2023) show variance on the 1 per cent level in the halo mass at $z = 0$ for Milky Way-like galaxies, similar to our simulations. Moreover, they show an average variance in the stellar mass of Milky Way-like galaxies on the 10 per cent level (EAGLE) and between 5 per cent and 10 per cent (SWIFT–EAGLE), again slightly larger than for our single galaxy.

These differences should motivate us to include similar robustness and convergence studies when designing new galaxy formation models, in particular for cosmological zoom simulations. Ideally, this would allow us to increase the robustness of a model not only at fixed resolution, but also when changing the numerical resolution. As one specific consequence of the study presented here, we will introduce a new approach that improves the stellar mass resolution in cosmological galaxy simulations, but avoids systematically changing galaxy properties at the same time (Pakmor et al. 2025).

ACKNOWLEDGEMENTS

RB was supported by the UZH Postdoc Grant (grant no. FK-23116) and the SNSF through the Ambizione Grant (PZ00P2_223532). RJJG acknowledges support from an STFC Ernest Rutherford Fellowship (ST/W003643/1). FvdV was supported by a Royal Society University Research Fellowship (URF\R1\191703 and URF\R\241005). FF was supported by a UKRI Future Leaders Fellowship (grant no. MR/X033740/1). The authors gratefully acknowledge the Gauss Centre for Supercomputing e.V. (www.gauss-centre.eu) for compute time on the GCS Supercomputer SUPERMUC-NG at Leibniz Supercomputing Centre (www.lrz.de).

DATA AVAILABILITY

The data underlying this article will be shared on reasonable request to the corresponding author.

REFERENCES

Bieri R., Pakmor R., van de Voort F., Talbot R. Y., Werhahn M., Pfrommer C., Springel V., 2025, preprint (arXiv:2509.07124)
Borrow J., Schaller M., Bahé Y. M., Schaye J., Ludlow A. D., Ploeckinger S., Nobels F. S. J., Altamura E., 2023, MNRAS, 526, 2441
Buck T., Pfrommer C., Pakmor R., Grand R. J. J., Springel V., 2020, MNRAS, 497, 1712
Crain R. A., van de Voort F., 2023, ARA&A, 61, 473
Davé R., Anglés-Alcázar D., Narayanan D., Li Q., Rafieferantsoa M. H., Appleby S., 2019, MNRAS, 486, 2827
Davies J. J., Crain R. A., Pontzen A., 2021, MNRAS, 501, 236
Davies J. J., Pontzen A., Crain R. A., 2022, MNRAS, 515, 1430
Dubois Y., Peirani S., Pichon C., Devriendt J., Gavazzi R., Welker C., Volonteri M., 2016, MNRAS, 463, 3948
Fragkoudi F., Grand R. J. J., Pakmor R., Springel V., White S. D. M., Marinacci F., Gomez F. A., Navarro J. F., 2021, A&A, 650, L16
Fragkoudi F., Grand R. J. J., Pakmor R., Gómez F., Marinacci F., Springel V., 2025, MNRAS, 538, 1587
Gargiulo I. D. et al., 2019, MNRAS, 489, 5742
Genel S. et al., 2019, ApJ, 871, 21
Gómez F. A., White S. D. M., Marinacci F., Slater C. T., Grand R. J. J., Springel V., Pakmor R., 2016, MNRAS, 456, 2779
Gómez F. A., White S. D. M., Grand R. J. J., Marinacci F., Springel V., Pakmor R., 2017, MNRAS, 465, 3446
Grand R. J. J. et al., 2017, MNRAS, 467, 179
Grand R. J. J. et al., 2021, MNRAS, 507, 4953
Hopkins P. F. et al., 2020, MNRAS, 492, 3465
Irodotou D. et al., 2022, MNRAS, 513, 3768
Joshi G. D., Pontzen A., Agertz O., Rey M. P., Read J., Renaud F., 2024, MNRAS, 528, 2346
Keller B. W., Wadsley J. W., Wang L., Kruijssen J. M. D., 2019, MNRAS, 482, 2244
Marinacci F., Pakmor R., Springel V., 2014, MNRAS, 437, 1750
Martin-Alvarez S., Sijacki D., Haehnelt M. G., Farcy M., Dubois Y., Belokurov V., Rosdahl J., Lopez-Rodriguez E., 2023, MNRAS, 525, 3806
Monachesi A., Gómez F. A., Grand R. J. J., Kauffmann G., Marinacci F., Pakmor R., Springel V., Frenk C. S., 2016, MNRAS, 459, L46
Monachesi A. et al., 2019, MNRAS, 485, 2589
Nelson D. et al., 2019, Comput. Astrophys. Cosmol., 6, 2
Pakmor R., Marinacci F., Springel V., 2014, ApJ, 783, L20
Pakmor R., Springel V., Bauer A., Mocz P., Munoz D. J., Ohlmann S. T., Schaal K., Zhu C., 2016, MNRAS, 455, 1134

Pakmor R. et al., 2017, MNRAS, 469, 3185
Pakmor R., Guillet T., Pfrommer C., Gómez F. A., Grand R. J. J., Marinacci F., Simpson C. M., Springel V., 2018, MNRAS, 481, 4410
Pakmor R. et al., 2020, MNRAS, 498, 3125
Pakmor R. et al., 2023, MNRAS, 524, 2539
Pakmor R. et al., 2024, MNRAS, 528, 2308
Pakmor R. et al., 2025, preprint (arXiv:2507.22104)
Pillepich A. et al., 2018, MNRAS, 475, 648
Rey M. P. et al., 2023, MNRAS, 521, 995
Riley A. H. et al., 2025, MNRAS, 542, 2443
Rodríguez Montero F., Martin-Alvarez S., Slyz A., Devriendt J., Dubois Y., Sijacki D., 2024, MNRAS, 530, 3617
Schaye J. et al., 2015, MNRAS, 446, 521
Sellwood J. A., Debattista V. P., 2009, MNRAS, 398, 1279
Shipp N. et al., 2025, MNRAS, 542, 1109
Simpson C. M., Grand R. J. J., Gómez F. A., Marinacci F., Pakmor R., Springel V., Campbell D. J. R., Frenk C. S., 2018, MNRAS, 478, 548
Simpson C. M. et al., 2019, MNRAS, 490, L32
Springel V., 2005, MNRAS, 364, 1105
Springel V., 2010, MNRAS, 401, 791
Springel V., Hernquist L., 2003, MNRAS, 339, 289
Springel V. et al., 2005, Nature, 435, 629
Springel V., Frenk C. S., White S. D. M., 2006, Nature, 440, 1137
Springel V. et al., 2008, MNRAS, 391, 1685
Springel V. et al., 2018, MNRAS, 475, 676
Springel V., Pakmor R., Zier O., Reinecke M., 2021, MNRAS, 506, 2871
van de Voort F., Bieri R., Pakmor R., Gómez F. A., Grand R. J. J., Marinacci F., 2021, MNRAS, 501, 4888
Vera-Casanova A. et al., 2025, preprint (arXiv:2503.17202)
Villaescusa-Navarro F. et al., 2021, ApJ, 915, 71
Vogelsberger M., Genel S., Sijacki D., Torrey P., Springel V., Hernquist L., 2013, MNRAS, 436, 3031
Vogelsberger M. et al., 2014, Nature, 509, 177
Vogelsberger M., Marinacci F., Torrey P., Puchwein E., 2020, Nat. Rev. Phys., 2, 42
Weinberger R., Springel V., Pakmor R., 2020, ApJS, 248, 32
Whittingham J., Sparre M., Pfrommer C., Pakmor R., 2021, MNRAS, 506, 229
Whittingham J., Sparre M., Pfrommer C., Pakmor R., 2023, MNRAS, 526, 224

This paper has been typeset from a TEX/LATEX file prepared by the author.